Soft Matter

PAPER

View Article Online
View Journal | View Issue

Cite this: *Soft Matter*, 2016, **12**, 9238

Phase diagram of binary colloidal rod-sphere mixtures from a 3D real-space analysis of sedimentation–diffusion equilibria†

Henriëtte E. Bakker,* Simone Dussi, Barbera L. Droste, Thijs H. Besseling, Chris L. Kennedy, Evert I. Wiegant, Bing Liu,‡ Arnout Imhof, Marjolein Dijkstra and Alfons van Blaaderen*

Received 22nd September 2016, Accepted 24th October 2016

DOI: 10.1039/c6sm02162j

www.rsc.org/softmatter

Self-assembly of binary particle systems offers many new opportunities for materials science. Here, we studied sedimentation equilibria of silica rods and spheres, using quantitative 3D confocal microscopy. We determined not only pressure, density and order parameter profiles, but also the experimental phase diagram exhibiting a stable binary smectic liquid-crystalline phase (Sm_2). Using computer simulations we confirmed that the Sm_2-phase can be stabilized by entropy alone, which opens up the possibility of combining new materials properties at a wide array of length scales.

Introduction

Three-dimensional structuring of matter on multiple length scales is key to the design of materials with new properties such as a photonic band gap[1] or a negative refractive index.[2] Self-assembly holds great promise of arriving at such materials in an affordable and sustainable way.[1–3] Self-assembly of multiple components such as in colloidal binary crystals increases the complexity of the structures and hence, the ability to tune the properties. Binary mixtures of colloidal rods and spheres have hardly been investigated experimentally,[4–6] despite the existence of a significantly larger number of theoretical and simulation studies.[7–20]

In this paper we study through experiments and simulations a binary mixture of rod-like and spherical colloids as shown in Fig. 1a and b. We consider mixtures of fluorescent silica rods and silica spheres, which enables us to determine the positions and orientations of individual particles in 3D. Real-space imaging has been done before on a similar system, but not a quantitative 3D analysis.[4,6] Using real-space analysis, we determine for the first time thermodynamic quantities such as osmotic pressure, local and global order parameters. With these, we map the experimental phase diagram of the binary silica rod-sphere mixture. As a result, it is possible to compare the experimental results directly with simulations and existing theories that use these thermodynamic quantities. We find the spontaneous formation of a binary smectic liquid-crystalline (Sm_2) phase in which smectic layers of rods alternate with layers of spheres (see Fig. 1c and 2). Since the smectic organisation arises in a two-component system, differently from the common lamellar order that occurs in single-component systems, we prefer to use the notation Sm_2. Note that in few papers this notation implies that the smectic phase is biaxial,[21] but this is not the case here. The first experimental Sm_2-phase was observed by Adams *et al.* in a mixture of *fd*-viruses (of end-to-end length to diameter ratio $L/D \sim 100$) and polymer spheres.[4] The stabilization mechanism was explained in terms of excluded-volume interactions, despite the fact that under particular conditions the chirality and flexibility of the *fd*-viruses play an important role in determining the phase behaviour.[22] In contrast, in the present system the rods are rigid and achiral, and we tailored the particle interactions to have only short-range repulsion between the colloids. This allows us to definitively confirm that the Sm_2-phase can be stabilized by entropy alone, as we also verified by performing computer simulations.

Material and methods

Colloid synthesis

Fluorescein isothiocyanate (FITC) fluorescently labeled silica rods were prepared according to the method of Kuijk *et al.*[23,24] 80.0 gram of poly(vinyl-pyrrolidone) (PVP, average molecular

---

Soft Condensed Matter, Debye Institute for Nanomaterials Science, Utrecht University, Princetonplein 5, 3584 CC Utrecht, The Netherlands. E-mail: henriette.bakker@gmail.com, a.vanblaaderen@uu.nl

† Electronic supplementary information (ESI) available: Details of the experiments, the simulations, local order parameters, the analysis and additional figures. See DOI: 10.1039/c6sm02162j

‡ Present address: State Key Laboratory of Polymer Physics and Chemistry, Institute of Chemistry, Chinese Academy of Sciences, No. 2 1st North Street Zhongguancun, Beijing, 100190, China.

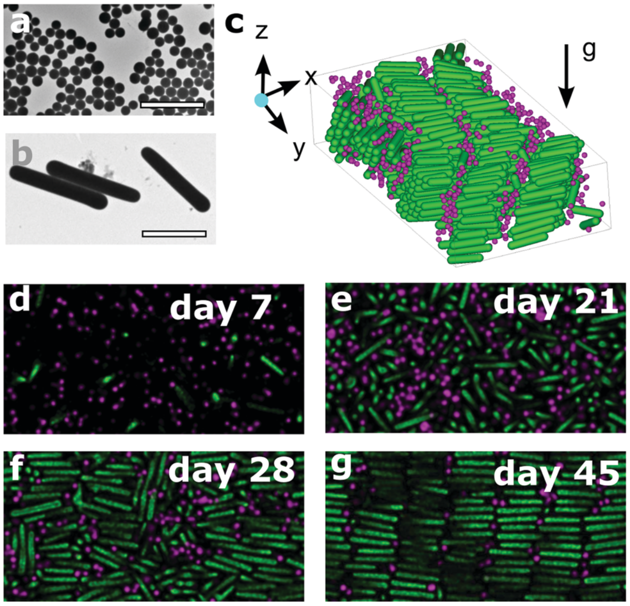

Fig. 1 3D single-particle analysis of a Sm_2-phase. (a and b) TEM images of (a) 385 nm silica spheres (polydispersity $\delta_\sigma \simeq 9\%$) and (b) silica rods with end-to-end length L = 3.6 μm ($\delta_L \simeq 18\%$) and diameter D = 0.59 μm ($\delta_D \simeq 10\%$), scale bars 2.5 μm. (c) 3D reconstruction from fitted particles of a part of a confocal data stack showing a Sm_2-phase. (d–g) Formation of the Sm_2-phase in a rod-sphere mixture over time, images taken at height ~17 μm.

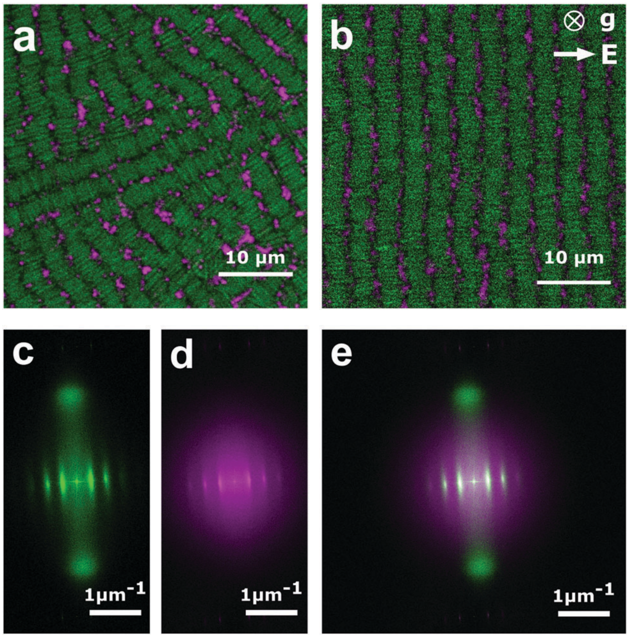

Fig. 2 Longe-range ordering of the Sm_2-phase using an electric field. (a) Binary smectic phase assembled without alignment by a field. (b) Confocal image of a part of the sample four days after the electric field had been turned off. For a zoom-out confocal image, see ESI,† Fig. S4. An ac-electric field (15 V mm^{-1}, 1 MHz) was applied for 48 hours during sedimentation of a sample ($\phi \approx 1.5$ vol% particles) with rods (R1, L/D = 5.6, L = 2.9 μm) and small spheres (σ = 385 nm). (c–e) FFT-images of the aligned binary smectic Sm_2-phase (0.5 mm × 0.7 mm), FFT-images are displayed on a logarithmic intensity scale. (c) FFT-image of the rod channel (d) FFT-image of the sphere channel (e) overlay of the FFT-images of both the green ((c) rod) and magenta ((d) sphere) channel.

weight M_w = 40 000 g mol^{-1}, Sigma-Aldrich) was dissolved in 800.0 mL of 1-pentanol (99%, Sigma-Aldrich) by sonication. After all PVP was dissolved, 80.0 mL of absolute ethanol (Baker), 20 mL of ultrapure water (Millipore) and 8.0 mL of 0.18 M sodium citrate dihydrate solution (99%, Sigma-Aldrich) were added and the flask was shaken by hand. Then 16.0 mL of aqueous ammonia solution (25 wt%, Merck) was added and the flask was shaken again. Next, 8.0 mL of tetraethylorthosilicate (TEOS, 98%, Sigma-Aldrich) was added. The mixture was shaken again and then allowed to react undisturbed for 72 h. The mixture was centrifuged at 2000 rpm for 30 minutes (Hettich rotina 46 s or Eppendorf 5810 centrifuge) to separate the silica rods. Afterwards, the silica rods were washed with ethanol twice, ultrapure water twice and ethanol twice, respectively. To grow a fluorescent silica shell around the rods, half of the prepared silica rods were dispersed into 300.0 mL ethanol containing 20.0 mL of ultrapure water and 24.0 mL of aqueous ammonia solution (25 wt%), under gentle magnetic stirring in a round-bottom flask. Subsequently, 0.750 mL of TEOS and 5.0 mL of a dye mixture were added. The reaction was stirred for 6 hours. The dye mixture was prepared the day before. For this mixture 25.0 mg (0.064 mmol) of fluorescein isothiocyanate (FITC, isomer I, 90%, Sigma-Aldrich) was dissolved in 5.0 mL absolute ethanol by sonication. Subsequently, 37.0 μL (0.16 mmol) of 3-aminopropyltriethoxysilane (APS, 99%, Sigma-Aldrich) was added. The dye mixture was left to react overnight, before adding it to the reaction mixture. Afterwards, the silica rods were washed twice with ethanol. Additional non-fluorescent silica shells were needed to enable single-particle tracking. To grow a non-fluorescent shell, we used a similar procedure without the addition of the dye-mixture. The procedure was repeated several (5 to 6) times to obtain a thick enough non-fluorescent shell. The final colloidal silica rods had a multi-layered structure: non-fluorescent silica core, fluorescently labeled silica shell (*ca.* 35 nm) and a non-fluorescent silica shell (*ca.* 145 nm).

Rhodamine isothiocyanate (RITC) fluorescently labeled silica spheres were prepared *via* a modified Stöber synthesis.[25]

In order to measure the dimensions of the as-prepared particles, transmission electron microscopy (TEM) images were made with a Philips Tecnai 10 or 12 microscope (FEI company). Typically 80 particles were measured by hand in the program iTEM (Soft Imaging System GmbH, Version 5.0). The average end-to-end length L, the average diameter D of the rods, and the average diameter σ of the spheres were measured. After which the aspect-ratio L/D and the polydispersity δ were calculated. The polydispersity is defined as $\delta_L = s_L/L$, with s_L the standard deviation of L.

For self-assembly using an electric field, colloidal silica rods with the following dimensions were used: R1 rods; L = 2860 nm and D = 510 nm (L/D = 5.6, δ_L = 9%, δ_D = 9%). For single-particle tracking the following colloidal silica rods were used: R2 rods with L = 3591 nm and D = 587 nm (L/D = 6.1, δ_L = 18%, δ_D = 10%). For all experiments, colloidal silica spheres with σ = 385 nm (δ = 9%) were used. See Fig. S1 for TEM images and Table S1 for more particle properties (ESI†).

Dispersions

For self-assembly using an ac-electric field, silica spheres and R1 silica rods were dispersed in a refractive index matched solvent mixture, n_D^{21} = 1.46, of 78 wt% dimethylsulfoxide (DMSO, ≥99.9%, Sigma-Aldrich) and 22 wt% ultrapure water.

For samples that were in sedimentation–diffusion equilibrium (SDE) of which single-particle fitting was needed, particles were dispersed in an index matched solvent mixture, n_D^{21} = 1.45, of 85 wt% glycerol (≥99.0%, Sigma-Aldrich) and 15 wt% ultrapure water. The mixture has a relatively high viscosity (81 mPa s, 25 °C).[26] This high viscosity causes the dynamics in the samples to slow down, this is especially important for imaging in the dilute top region, where the dynamics are fastest. In order to control the thickness of the double layer around the particles, Lithium Chloride salt (LiCl, Merck) was added to a concentration of 0.55 mM to the glycerol–water mixture. Taking a dielectric constant of $\varepsilon_r = 49.6\varepsilon_0$ for the solvent mixture, based on a linear interpolation of literature values,[27] the typical Debye screening length (κ^{-1}) in this solution is estimated to be 10 nm.

The Debye screening length can be calculated from

$$\kappa^{-1} = \sqrt{8\pi\lambda_b c} \tag{1}$$

where,

$$\lambda_b = \frac{e^2}{4\pi\varepsilon_r\varepsilon_0 k_B T} \tag{2}$$

Here, λ_b is the Bjerrum length, c is the salt concentration in mol m^{-3}, and ε_r and ε_0 are the dielectric constant of the solvent and the permittivity of vacuum, e is the elementary charge, k_B is Boltzmann's constant and T is the absolute temperature.

Confocal microscopy

Samples were studied with a Laser Scanning Confocal Microscope (Leica TCS SP2 and Leica TCS SP8, equipped with a 12 kHz resonant scanner). All images were taken in fluorescence mode. The excitation wavelength was 488 nm for the FITC-labeled rods and 543 nm for the RITC-labeled spheres. To optimize image quality, a 100×, 1.35 NA glycerol confocal-objective (Leica) was used for single-particle tracking in combination with a quartz coverslip (n_D = 1.46, 0.15–0.18 mm, Laser Optex). For other purposes, oil objectives were used: either a 100×, 1.3 NA oil confocal-objective (Leica) or a 63×, 1.4 NA oil confocal-objective (Leica). A typical image volume had the following dimensions ∼25 μm × 12.5 μm × 120 μm. We imaged with a voxel size of ∼50 nm × 50 nm × 100 nm. Data shown here are averaged for at least 4 different confocal *xyz*-stacks, which were recorded consecutively or at different places in the sample.

Sample cells

For self-assembly using an ac-electric field the sample cell was prepared using two 50 μm diameter nickel alloy wires (Goodfellow) running on opposite sides through a 0.1 mm × 1 mm rectangular glass capillary (Vitrocom, UK) and glued to a standard microscopy slide (Menzel Gläzer). The distance between the wires was around 0.7 mm. The cell was filled with particles dispersed in an index matched solvent mixture of 78 wt% DMSO–water and sealed with UV-glue (Norland, No. 68). The samples were left to sediment with the long axis perpendicular to gravity. See Fig. S2 for a schematic (ESI†).

For SDE samples of which single-particle fitting was needed, the following sample cell was made. First, the back-end of a glass Pasteur pipette (WU Mainz) was cut off using a diamond pen. Afterwards, the resulting glass cylinder (∅ 5 mm) was glued on top of a quartz coverslip using UV-glue. Next, the glass cylinder was slid through a circular hole of 7 mm that was drilled in the middle of a standard microscopy slide. Then, the cylinder was attached permanently by gluing the coverslip to the microscopy slide. The sample cells were filled with 150 μL dispersion containing ∼0.5 vol% particles, total height of the dispersion was ∼6 mm. The cells were closed with cotton wool wrapped in laboratory film (Parafilm) and sealed with candle wax. See Fig. S3 for a schematic (ESI†).

Electric field assembly

A sinusoidal signal of 1 MHz and an amplitude of 3.0 V was generated using a function generator (Agilent, 33120A). This signal was then sent to the sample *via* a wide band amplifier (Krohn-Hite, 7602M), that was used to control the electric field strength in the sample cell. An electric field of 15 V mm^{-1} was applied for 48 hours while the sample was left to sediment, then the electric field was switched off. Four days after the electric field was switched off, the sample was imaged with the confocal microscope.

Six confocal images were made over an area of 0.5 mm × 0.7 mm, using the 'tile scan' option in the Leica LASAF 4.1 software. Of each of the images and each of the two separate channels of the confocal images a fast Fourier transform (FFT) image was made. This was done using the algorithm in ImageJ software (1.49m, NIH). The FFT images of one channel were combined by adding up the intensities from the six separate FFT images. This resulted in one combined FFT image from the rod channel and one image from the sphere channel. One overview image was created from the six confocal images by using the stitch procedure in the Leica LASAF software.

Measuring the translational diffusion constant

We followed the diffusion of spherical particles inside the Sm$_2$-phase, in a sediment of R1 rods and spheres at SDE. We measured inside the Sm$_2$-phase at a height close to the transition between the isotropic and Sm$_2$-phase. We recorded with the confocal microscope *xyt*-series, with a length of 1200 frames and an interval Δt = 90 ms. The *xy*-plane was chosen such that the *y*-axis corresponded to the nematic director $\hat{n}$ of the Sm$_2$-phase. We obtained 2D trajectories of the particles from the recorded images using particle fitting and tracking algorithms.[28] Next, we calculated the mean square displacement (MSD) as a function of time. To obtain values for the translational diffusion constant D_t inside the Sm$_2$-phase we fitted

$$\langle \Delta r^2(t) \rangle = 2dD_t t + 4{\varepsilon_t}^2 \tag{3}$$

to the plot of the MSD *versus* time t. Here $\langle \Delta r^2(t) \rangle$ is the MSD, d the dimensionality of the track and ε_t is the error of the measurement.[29]

Single-particle fitting algorithms and data analysis

Confocal data was deconvolved using commercially available Huygens SVI software (Version 14.10), using a theoretical point spread function (PSF). This theoretical PSF was close to the measured PSF.[30] The rod fitting algorithm of Besseling *et al.* was used to identify the positions and orientations of the rods.[31] The positions of the spheres were obtained using an algorithm similar to the method of Crocker and Grier[28] but extended to 3D.[32] For analysis, the experimental coordinate data were first divided into equally spaced slabs of 0.5D along the gravity direction, with D the average bare rod diameter, followed by calculation of the number density (ρ), composition (x), and osmotic pressure (P) for each slab. Pressures P at height z were calculated by integrating the density profiles of both species to obtain the weight of all particles above

$$P(z) = \Delta\rho v_{\mathrm{sph}} g \int_z^h \rho_{\mathrm{sph}}(z)\mathrm{d}z + \Delta\rho v_{\mathrm{rod}} g \int_z^h \rho_{\mathrm{rod}}(z)\mathrm{d}z, \tag{4}$$

with $\Delta\rho = \rho_{\mathrm{particle}} - \rho_{\mathrm{solvent}}$ the apparent density of the silica particles, v_{sph} and v_{rod} the volume of one sphere or rod, respectively, ρ_{sph} and ρ_{rod} the local particle number density of the spheres or rods, respectively, and h height of the sampled volume, where we made sure that at SDE the particle density vanished at h. The local nematic order parameter S_i and the local smectic order parameter τ_i were calculated for each particle i. Successively, the averaged values $\langle S_i \rangle$ and $\langle \tau_i \rangle$ were calculated for each slabs by considering only the particles in the given slab. See ESI† for details on the nematic S_i and smectic τ_i local order parameter.

Monte Carlo simulations

The colloidal silica spheres and rods are modeled as hard spheres of diameter σ and hard spherocylinders of (cylinder) length L_{cyl} and diameter D, respectively. Notice that the experimental end-to-end length L is defined as $L = L_{\mathrm{cyl}} + D$. Particles interact *via* a purely excluded-volume pair potential: $U = \infty$ if two particles overlap, $U = 0$ otherwise. We first perform Monte Carlo (MC) simulations in the *NPT* ensemble of 1600 hard spherocylinders to map the behaviour of the experimental (single-component) system of silica rods onto hard-particle behaviour, *i.e.*, identify the effective dimensions of the silica rods (see SI 1 and Fig. S7 in ESI†). After this analysis, we simulate $N_{\mathrm{tot}} = N_{\mathrm{sph}} + N_{\mathrm{rods}} = 3125$ hard spheres and hard spherocylinders ($L_{\mathrm{cyl}} = 6.46\sigma$, $D = 1.52\sigma$, $L_{\mathrm{cyl}}/D \sim 4.25$) in the *NPT* ensemble with various composition $x_{\mathrm{sph}} = N_{\mathrm{sph}}/N_{\mathrm{tot}}$. Each simulation consists of several million of MC steps, where one step is defined as N_{tot} moves randomly chosen from sphere translation, rod translation, rod rotation, and either isotropic or anisotropic change of the simulation box volume. Initial configurations at a given composition x_{sph} are obtained from an equilibrated configuration at lower x_{sph} by replacing an appropriate number of rods with spheres. Each state point has been analysed by suitable combinations of order parameters that allowed us to identify the liquid-crystalline bulk behaviour of the mixture as reported in Fig. 5. See SI 4 in ESI† for more details.

Results and discussion

We synthesized silica spheres with an average bare diameter of $\sigma = 385$ nm (polydispersity $\delta_\sigma \simeq 9\%$) and two batches of silica rods; R1 rods with bare length $L = 2.9$ μm ($\delta_L \simeq 9\%$) and bare diameter $D = 0.51$ μm ($\delta_D \simeq 9\%$) and R2 rods with bare length $L = 3.6$ μm ($\delta_L \simeq 18\%$) and bare diameter $D = 0.59$ μm ($\delta_D \simeq 10\%$),[23,24] see Fig. 1a and b (Fig. S1 in ESI†). Colloidal rods and spheres were designed to interact as nearly hard particles with slightly larger effective dimensions, see SI 1 in ESI† for details. The silica rods and spheres ($\rho \sim 2$ g mL^{-1}) are not density-matched with the solvent mixture ($\rho \sim 1$ g mL^{-1}). Hence, at sedimentation–diffusion equilibrium most of the rods (R2, $l_{\mathrm{g}} = 0.64$ μm) reside at the bottom of the sediment and most of the spheres ($l_{\mathrm{g}} = 17.65$ μm) at the top, due to difference in gravitational height l_{g} between the particles. At intermediate heights, (for example $h \sim 17$ μm, see Fig. 1d–g), both species were present and over time a Sm$_2$-phase was formed.

In most of the samples, the Sm$_2$-phase was not present as one single, large domain. Rather, we observed Sm$_2$-domains with different orientations throughout the sample, as illustrated in Fig. 2a. In order to show that the observed Sm$_2$-phase is stable, we aligned the Sm$_2$-phase by applying a relatively small ac-electric field to the sample, which induced a dipole moment in each rod due to the dielectric constant mismatch between the rods and the solvent.[33] Our binary colloidal system responded by aligning its director to the electric field, over macroscopically (mm^2) large areas, whereas the spheres remained in between the smectic layers of rods, Fig. 2b. For a zoom-out see Fig. S4 in ESI.† The alignment of the rods with the electric field was still preserved 4 days after turning off the field, although minor undulations in the smectic layers were observed. From these observations we conclude that the Sm$_2$-phase is a stable phase.

To further characterize the order in the aligned Sm$_2$-phase, fast Fourier transform (FFT) images were made from the tiles of the zoom-out image presented in ESI,† Fig. S4. The FFT image of the rod channel (Fig. 2c) shows that the rods are organized in a smectic phase, in one single domain. Moreover, one characteristic length scale can be observed corresponding to the transverse distance between the rods in the smectic layers and one characteristic length scale associated to the spacing between the smectic layers. The FFT image of the sphere channel (Fig. 2d) shows only one characteristic length scale corresponding to the spacing between sheets of spheres. No long-range order of the spheres was observed within the sheet of spheres, and the observed dynamics was that of a 2D liquid. In Fig. 2e the FFT images of both the rod and the sphere channel are merged into one single image. The ease of alignment and formation of the Sm$_2$-phase during sedimentation is

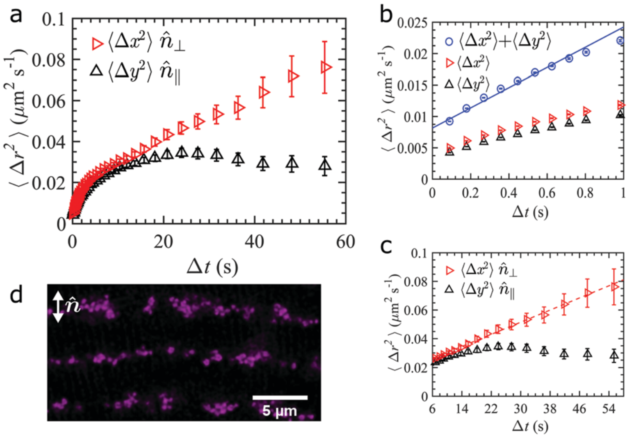

Fig. 3 Mean square displacement inside the Sm$_2$-phase. (a) Measured MSD parallel to the nematic director (Δ) and perpendicular to the nematic director (▷). (b) Same as (a) but for $\Delta t < 1$ s. The solid line is a linear fit through $\langle \Delta r^2 \rangle$ for $t < 1$ s using eqn (3). (c) Same as (a) but for $\Delta t > 6$ s. The dashed line is a linear fit through the MSD perpendicular to the nematic director for $t > 6$ s using eqn (3). (d) Confocal snapshot taken from the recorded *xyt*-series. The double arrow denotes the nematic director $\hat{n}$, that identifies the average orientation of the rods. Only the spheres were imaged for this measurement.

important for use in applications. It is expected that such alignment with relatively small fields will work equally well for Sm$_2$-phases of particles with nanometer size.

In order to show that the Sm$_2$-phase was still dynamic and not kinetically arrested we measured the mean square displacement (MSD) of the spheres inside a sediment of the Sm$_2$-phase, see Fig. 3. The black symbols depict the MSD measured along the nematic director and the red symbols depict the MSD measured perpendicular to the nematic director. In Fig. 3d a confocal snapshot is shown from the recorded *xyt*-series of the spheres inside the Sm$_2$-phase, the double arrow denotes the nematic director $\hat{n}$. Fig. 3b shows that at $t < 1$ s, the short time self-diffusion was on average the same in both directions. The spheres were not hindered by the smectic layers of rods at $t < 1$ s. We fitted $\langle \Delta r^2 \rangle = \langle \Delta x^2 \rangle + \langle \Delta y^2 \rangle$ for $t < 1$ s to equation 3 with $d = 2$, to obtain the short time self-diffusion coefficient. We found a short time self-diffusion coefficient $D^s_{t<1} = (4.00 \pm 0.21) \times 10^{-3}$ μm s^{-1}, with $\varepsilon_t = 45$ nm. We compared the short time self-diffusion coefficient with the diffusion coefficient of spheres measured in a dilute suspension. For a dilute suspension of spheres we obtained $D^0_t = (1.300 \pm 0.016) \times 10^{-2}$ μm s^{-1}, with $\varepsilon_t = 38$ nm, see Fig. S12 in ESI.† The measured $D^s_{t<1}$ inside the Sm$_2$-phase was 1/3 of the D^0_t in a dilute suspension of spheres. This is reasonable as the hydrodynamic coupling close to neighboring particles tends to slow down self-diffusion.[34] It is known for only hard spheres that the short time self-diffusion coefficient at $\phi = 0.4$ is reduced to $\sim 1/3\ D^0_t$.

When $t > 1$ s, the diffusion in both directions slowed down. We observed that at longer time scales ($t > 10$ s) the MSD parallel to the nematic director reached a plateau. This is expected, because the diffusion of spheres along the nematic director is hindered due to the presence of smectic layers of rods. In contrast, the diffusion perpendicular to the nematic director was not hindered. Still, the self-diffusion at longer time scales ($t > 6$ s) became slower due to the presence of other spheres. By fitting equation 3 through the MSD perpendicular to the nematic director for $t > 6$ s, a long-time self diffusion coefficient was obtained of $D_{t>6} = (0.5 \pm 0.09) \times 10^{-3}$ μm s^{-1}, see Fig. 3c. After 55 seconds the spheres had diffused on average 275 nm in the direction perpendicular to the nematic director. This distance is greater than the sphere's own radius, which further confirms that the Sm$_2$-phase observed is in equilibrium. These observations are in agreement with recent simulations,[35] in which also hindered diffusion of spheres parallel to the nematic director was observed. Additionally, they predicted the hopping of spheres between smectic layers. However, as we were only able to track the spheres over relatively short time scales, we were not able to experimentally verify this hopping of spheres.

In order to determine the thermodynamic properties of the Sm$_2$-phase, we performed a real-space analysis of binary rod-sphere mixtures in sedimentation–diffusion equilibrium. Sedimentation enables us to probe the phase behaviour and thermodynamics of the system over a wide range of system parameters in just one single experiment. We let our samples sediment for at least four weeks. The equilibrated samples had a final sediment height of around 100 μm. We optimized our system for single-particle tracking and used a fast scanning confocal microscope. After deconvolution of the images we used single-particle identification algorithms[31] to obtain the positions and orientations of all particles individually. Using these coordinates, we determined the number density of the rods $\rho_{\text{rod}}(z)$ and of the spheres $\rho_{\text{sph}}(z)$ as a function of height z in the sediment. Using not only the positions but also the orientations of the rods allowed us to determine the average local nematic $\langle S_i \rangle(z)$ and smectic $\langle \tau_i \rangle(z)$ order parameter profiles as a function of z, where the brackets denote an average over all particles in the slab at z, see SI 2 in ESI† for details on the local order parameters. In Fig. 4a, we plot both the composition ($x_{\text{sph}} = N_{\text{sph}}/N_{\text{tot}}$), with N_{sph} and N_{tot} the number of spheres and the total number of particles, respectively, as well as the order parameters as function of z. For comparison, the deconvolved confocal *xyz*-stack is presented in Fig. 4b. We clearly observe a rod-rich smectic phase, *i.e.*, $x_{\text{sph}} \simeq 0.4$, with high nematic order $\langle S_i \rangle > 0.9$ and high smectic order $\langle \tau_i \rangle > 0.6$ at the bottom of the sample. Whereas, an isotropic sphere-rich phase with $x_{\text{sph}} \sim 1$ and low nematic and smectic order is observed at the top. The transition between the isotropic and Sm$_2$-phase occurred at a height of $\sim$14 μm, see Fig. 4f. In order to distinguish the different phases, we did not use the positions of the spheres in the order parameter analysis, as the order of the spheres is dictated by that of the rods and is less pronounced (see Fig. S6 in ESI† for more details).

Finally, we mapped out the experimental phase diagram in the reduced osmotic pressure $\beta P D_{\text{eff}}^3$ – composition x_{sph} representation, by preparing and investigating many samples with different initial volume fractions and compositions, and by analyzing these using the same procedures as described above.

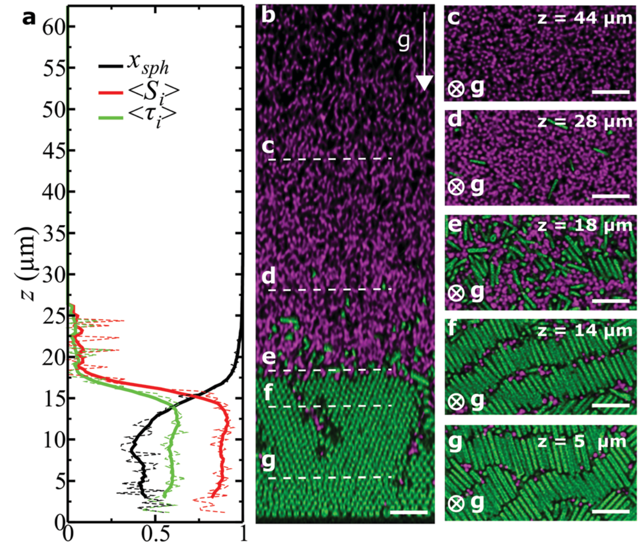

Fig. 4 (a) Quantitative analysis of local structure after determination of particle positions and orientations of an equilibrated sample. Plot of averaged local nematic $\langle S_i \rangle$ order parameter (red), averaged local smectic $\langle \tau_i \rangle$ order parameter (green) and composition $\langle x_{\mathrm{sph}} \rangle$ as a function of height z (black). Thin dashed lines are raw data divided in equally spaced slabs of 0.5D, along the gravity direction. Thick lines are data smoothed by convolution using a top-hat function of 5D width. (b–g) Deconvolved confocal microscopy images of a sediment of rods (R2) and spheres. Images are shown (b) parallel to gravity and (c–g) perpendicular to gravity. The dashed horizontal lines in (b) indicate the height at which the images (c–g) were acquired. All scale bars are 5 μm. The height of the total sediment was 120 μm, height shown here is 62.5 μm.

Here $\beta = 1/k_{\mathrm{B}}T$ denotes the inverse temperature with k_{B} Boltzmann's constant. To this end, we determined the osmotic pressure P at height z by integrating the density profiles of both species to obtain the weight of all particles above it. The osmotic pressure depends solely on the local densities of the spheres $\rho_{\mathrm{sph}}(z)$ and rods $\rho_{\mathrm{rod}}(z)$, yielding the equation of state P, in the ρ_{sph} and ρ_{rod} parameter space.

Every sample that reached SDE followed one sedimentation path through the two-dimensional reduced pressure $\beta PD_{\mathrm{eff}}{}^3$ – composition x_{sph} plane, Fig. 5. From the top of the sediment down, each path shows an initial increase in pressure at large x_{sph}, followed by a nearly horizontal portion in the $P(x_{\mathrm{sph}})$ curve, suggestive of a broad coexistence between a low density phase and a Sm$_2$-phase. Finally, in the Sm$_2$-phase the pressure rises, while x_{sph} decreases only slowly. Each path presents the expected sequence isotropic I–(nematic N)–binary smectic Sm$_2$ that was identified by employing the average nematic and smectic local order parameters. We used the following threshold values to determine the different phases; isotropic if $\langle S_i \rangle < 0.5$ and $\langle \tau_i \rangle < 0.35$, nematic if $\langle S_i \rangle > 0.5$ and $\langle \tau_i \rangle < 0.35$, Sm$_2$ if $\langle S_i \rangle > 0.5$ and $\langle \tau_i \rangle > 0.35$ (SI 3 in ESI†). We thus find a stable Sm$_2$-phase in our experimental phase diagram for sufficiently high pressures $\beta PD_{\mathrm{eff}}{}^3 > 3$ and compositions $0 \leq x_{\mathrm{sph}} \leq 0.8$ in binary silica rod-sphere mixtures. The sedimentation path at $x_{\mathrm{sph}} = 0$ shows that in sediment of only rods, with $L/D = 6.1$, also a smectic phase is formed. In between the smectic and isotropic phase a thin nematic layer of height $\Delta z = 1.5$ μm was present.

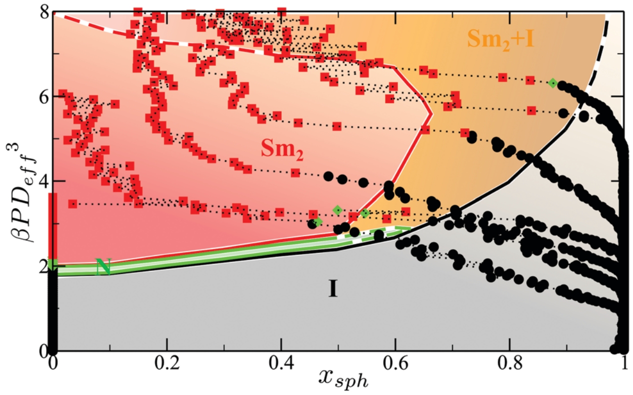

Fig. 5 Mapping of the experimental sedimentation paths (symbols) on the bulk phase diagram obtained from Monte Carlo simulations. The phase diagram as obtained from MC simulations of bulk mixtures of hard spherocylinders and hard spheres displays a stable isotropic I (grey), nematic N (green), binary smectic Sm$_2$ (red), and a I–Sm$_2$ coexistence region (orange). The symbols denote the experimental sedimentation paths in the reduced osmotic pressure $\beta PD_{\mathrm{eff}}{}^3$ – composition x_{sph} plane as obtained from different sediments of rods and spheres (symbols) and a sediment of only rods at $x_{\mathrm{sph}} = 0$. We used the following thresholds to determine in the experimental system the different liquid-crystal phases; I if $\langle S_i \rangle < 0.5$ and $\langle \tau_i \rangle < 0.35$ (black spheres), N if $\langle S_i \rangle > 0.5$ and $\langle \tau_i \rangle < 0.35$ (green diamonds), Sm$_2$ if $\langle S_i \rangle > 0.5$ and $\langle \tau_i \rangle > 0.35$ (red squares).

In order to explore the possibility that the Sm$_2$-phase coexists with a low-density phase and to investigate if the Sm$_2$-phase can be stabilized by entropy alone, we determined the phase diagram using Monte Carlo (MC) simulations of hard spherocylinders and hard spheres with the effective dimensions of the experimental particles. We estimated the effective diameter of the spheres σ_{eff} by mapping the equation of state of the spheres as obtained from the top part, which contained only spheres, of an equilibrated sediment to the Carnahan–Starling equation of state.[36] In addition, the effective dimensions of the rods, L_{eff} and D_{eff} were obtained by mapping the I–N transition as identified by the jump in the global nematic order parameter S in experimental data on a rods-only system to the transition as obtained from simulations (Fig. S7 in ESI†). We performed simulations in the *NPT* ensemble at many different state points and analyzed the phase behaviour by employing local and global nematic and smectic order parameters (see SI 4 in ESI† for details). In Fig. 5, we superimpose the experimental sedimentation paths on the phase diagram obtained by simulations. The topology of the phase diagram is consistent with previous theoretical studies[7] and shows a wide isotropic–binary smectic (I–Sm$_2$) coexistence region. We indeed confirm that the nearly horizontal parts of the experimental sedimentation paths agree qualitatively with the broad I–Sm$_2$ coexistence region as obtained from simulations. However, we note that $P(x_{\mathrm{sph}})$ should actually be horizontal due to the condition of equal pressure for the two coexisting phases, but are slightly slanted due to the finite interfacial width. We thus conclude that the observed experimental phase behaviour of silica rods and spheres is predominantly driven by entropy, and thus by the particle shape alone, which was to be expected as the van der Waals interactions can be neglected due to the refractive index-matching and the Coulombic interactions were screened by the addition of salt.

Moreover, we note that the theoretical phase diagram as obtained from MC simulations shows that the number of spheres in between the smectic layers of rods can be tuned in the Sm_2-phase as the composition ranges from $0 \leq x_{sph} \leq 0.6$, which is relevant for future application of these Sm_2-phases. We also mention that we did not observe any crystalline order in our samples likely due to the relatively high polydispersity in the length of the rods (δ_L = 18%) and in the diameter of the spheres (δ_σ = 9%). We expect to find stable crystal phases for systems with a lower polydispersity, see *e.g.* ref. 6.

Conclusions

Our results obtained from both experiments and simulations show that colloidal rods and spheres can spontaneously co-assemble in a binary liquid crystal phase, *i.e.*, a Sm_2-phase. Previous experimental work already showed the formation of the Sm_2-phase, but did not reveal the local structure on the single-particle level and did not study the phase diagram as function of pressure and composition.[4] We used fluorescently labeled silica particles to determine for the first time the structure and composition of the Sm_2-phase on the single-particle level using a combination of confocal microscopy and particle fitting algorithms.[31] In addition, we showed that the Sm_2-phase can be aligned with an ac-electric field. We also showed that inside the Sm_2-phase spheres still diffused freely. We investigated systems in sedimentation–diffusion equilibrium, which allowed us to determine the osmotic pressure at height z of the system, a quantity that is usually not accessible in experiments. Finally, we mapped out the experimental phase diagram in the pressure-composition representation. This allows for direct comparison with existing theory and our simulations and we find qualitative agreement with the phase diagram as obtained from simulations on mixtures of hard spherocylinders and hard spheres. The phase diagram exhibits a large stable region, where rods and spheres co-assemble in a single Sm_2-phase, which is surrounded by a huge demixing region at higher pressures and compositions x_{sph}. As the Sm_2-phase can be stabilized by entropy alone, we expect that this intriguing phase can be realized for a broad class of systems at many different length scales. Hence, the co-assembly of two particle shapes in a single phase allows us to take advantage of multiple species in a single material and the tunability of the positional and orientational order in liquid-crystalline phases. For instance, realizing an aligned Sm_2-phase of gold nanorods and spherical semiconductor particles using a small electric field is of great interest. The spherical semiconductor particles at the gold nanorod tips will experience strong plasmon enhanced electromagnetic fields that will enhance the luminescence of the semiconductor particles.

Acknowledgements

HEB, AvB and AI acknowledge financial support from the Foundation for Fundamental Research on Matter (FOM), in the Stirring of Light! program, which is part of the Netherlands Organisation for Scientific Research NWO. SD and MD acknowledge financial support from an NWO-CW-Echo grant. Part of the research leading to these results has received funding from the European Research Council under the European Unions Seventh Framework Programme (FP/2007-2013)/ERC Grant Agreement no. [291667:HierarSACol]. HEB performed the experiments under the supervision of AvB and AISD and HEB performed the order parameters analysis. SD carried out the simulations under the supervision of MD. THB helped to set-up the single-particle fitting analysis. CLK developed the set-up to measure the sedimentation–diffusion equilibria. BLD, EIW and BL performed preliminary experiments. The paper is co-written by HEB and SD, with contributions of AI, MD and AvB. All authors discussed results and revised the paper.

References

1 J. F. Galisteo-López, M. Ibisate, R. Sapienza, L. S. Froufe-Pérez, A. Blanco and C. López, *Adv. Mater.*, 2011, **23**, 30–69.
2 S. Mühlig, A. Cunningham, J. Dintinger, T. Scharf, T. Bürgi, F. Lederer and C. Rockstuhl, *Nanophotonics*, 2013, **2**, 211–240.
3 P. Podsiadlo, G. V. Krylova, A. Demortière and E. V. Shevchenko, *J. Nanopart. Res.*, 2010, **13**, 15–32.
4 M. Adams, Z. Dogic, S. L. Keller and S. Fraden, *Nature*, 1998, **393**, 349–352.
5 M. Adams and S. Fraden, *Biophys. J.*, 1998, **74**, 669–677.
6 X. Ye, J. a. Millan, M. Engel, J. Chen, B. T. Diroll, S. C. Glotzer and C. B. Murray, *Nano Lett.*, 2013, **13**, 4980–4988.
7 G. Cinacchi, E. Velasco and L. Mederos, *J. Phys.: Condens. Matter*, 2004, **16**, S2003–S2014.
8 A. Cuetos, B. Martínez-Haya, S. Lago and L. F. Rull, *Phys. Rev. E: Stat., Nonlinear, Soft Matter Phys.*, 2007, **75**, 1–12.
9 Z. Dogic, D. Frenkel and S. Fraden, *Phys. Rev. E: Stat. Phys., Plasmas, Fluids, Relat. Interdiscip. Top.*, 2000, **62**, 3925–3933.
10 R. van Roij, B. Mulder and M. Dijkstra, *Physica A*, 1998, **261**, 374–390.
11 S. K. Lai and X. Xiao, *J. Chem. Phys.*, 2010, **132**, 044905.
12 S. Varga, K. Purdy, A. Galindo, S. Fraden and G. Jackson, *Phys. Rev. E: Stat., Nonlinear, Soft Matter Phys.*, 2005, **72**, 1–19.
13 S. Varga, E. Velasco, L. Mederos and F. J. Vesely, *Mol. Phys.*, 2009, **107**, 2481–2492.
14 T. Koda, M. Numajiri and S. Ikeda, *J. Phys. Soc. Jpn.*, 1996, **65**, 3551–3556.
15 Y. Martinez-Raton, G. Cinacchi, E. Velasco and L. Mederos, *Eur. Phys. J. E: Soft Matter Biol. Phys.*, 2006, **21**, 175–188.
16 S. D. Peroukidis, A. G. Vanakaras and D. J. Photinos, *J. Mater. Chem.*, 2010, **20**, 10495.
17 D. Antypov and D. J. Cleaver, *Chem. Phys. Lett.*, 2003, **377**, 311–316.
18 S. Lago, A. Cuetos, B. Martínez-Haya and L. F. Rull, *J. Mol. Recognit.*, 2004, **17**, 417–425.
19 D. Antypov and D. J. Cleaver, *J. Chem. Phys.*, 2004, **120**, 10307–10316.

20 N. Urakami and M. Imai, *J. Chem. Phys.*, 2003, **119**, 2463.

21 G. W. G. H. W. S. V. V. Dietrich Demus, John W. Goodby, *Handbook of Liquid Crystals, Low Molecular Weight Liquid Crystals II*, Wiley-VCH, 1998, vol. 2B.

22 E. Grelet, *Phys. Rev. X*, 2014, **4**, 021053.

23 A. Kuijk, A. Imhof, M. H. W. Verkuijlen, T. H. Besseling, E. R. H. van Eck and A. van Blaaderen, *Part. Part. Syst. Charact.*, 2014, **31**, 706–713.

24 A. Kuijk, A. van Blaaderen and A. Imhof, *J. Am. Chem. Soc.*, 2011, **133**, 2346–2349.

25 N. A. M. Verhaegh and A. van Blaaderen, *Langmuir*, 1994, **10**, 1427–1438.

26 N.-S. Cheng, *Ind. Eng. Chem. Res.*, 2008, **47**, 3285–3288.

27 G. Akerlof, *J. Am. Chem. Soc.*, 1932, **54**, 4125–4139.

28 J. Crocker and D. Grier, *J. Colloid Interface Sci.*, 1996, **179**, 298–310.

29 T. Savin and P. S. Doyle, *Biophys. J.*, 2005, **88**, 623–638.

30 T. H. Besseling, J. Jose and A. Van Blaaderen, *J. Microsc.*, 2015, **257**, 142–150.

31 T. H. Besseling, M. Hermes, A. Kuijk, B. de Nijs, T. S. Deng, M. Dijkstra, A. Imhof and A. van Blaaderen, *J. Phys.: Condens. Matter*, 2014, **194109**, 1–12.

32 U. Dassanayake, S. Fraden and A. van Blaaderen, *J. Chem. Phys.*, 2000, **112**, 3851.

33 A. Kuijk, T. Troppenz, L. Filion, A. Imhof, R. van Roij, M. Dijkstra and A. van Blaaderen, *Soft Matter*, 2014, **10**, 6249–6255.

34 J. K. G. Dhont, *An Introduction to Dynamics of Colloids*, Elsevier, 1996.

35 M. Piedrahita, A. Cuetos and B. Martínez-Haya, *Soft Matter*, 2015, **11**, 3432–3440.

36 R. Piazza, T. Bellini and V. Degiorgio, *Phys. Rev. Lett.*, 1993, **71**, 4267–4270.